 doi:10.20944/preprints202108.0362.v1

Article

Photothermal Effects and Heat Conduction in Nanogranular Silicon Films

B.A. Kurbanova[1], G.K. Mussabek[2,3], V.Yu. Timoshenko[3,4,5], V. Lysenko[3,6] and Z.N. Utegulov[1,*]

[1] Department of Physics, School of Sciences and Humanities, Nazarbayev University, Nur-Sultan 010000, Kazakhstan; bayan.kurbanova@nu.edu.kz

[2]Faculty of Physics and Technology, Al-Farabi Kazakh National University, Almaty 050040, Kazakhstan; gauhar.musabek@kaznu.kz

[3] Institute of Engineering Physics for Biomedicine, Laboratory "Nanotheranostics", National Research Nuclear University "MEPhI", 115409 Moscow, Russia; victor_timoshenk@mail.ru

[4]Faculty of Physics, Lomonosov Moscow State University, 119899 Moscow, Russia;

[5] Lebedev Physical Institute of RAS, 119899 Moscow, Russia;

[6] Light Matter Institute, UMR-5306, Claude Bernard University of Lyon, 2 rue Victor Grignard, 69622 Villeurbanne, France; vladimir.lysenko@univ-lyon1.fr

[*]Correspondence: zhutegulov@nu.edu.kz

Abstract: We present the results on photothermal (PT) and heat conductive properties of *nanogranular silicon (Si)* films synthesized by evaporation of colloidal droplets (drop-casting) of 100 ± 50 nm sized crystalline Si nanoparticles (NP) deposited on glass substrates. Finite difference time domain (FDTD) and finite element mesh (FEM) modeling of absorbed light intensity and photo-induced spatial temperature distribution across the Si NP films were well correlated with the local temperatures measured by micro-Raman spectroscopy and used for determination of heat conductivities in the films of various thicknesses. Cubic-to-hexagonal phase transition in these films caused by laser heating was found to be heavily influenced by the film thickness and heat conductive properties of glass substrate, on which the films were deposited. Heat conductivities across the drop-casted Si *nanogranular* films were found to be in the range of lowest heat conductivities of other types of *nanostructurely voided* Si films due to enhanced phonon scattering across inherently voided topology, weak NP-NP and NP-substrate interface bonding within nanogranular Si films.

Keywords: silicon, nanogranular, nanoparticle, porous, void, thin film, laser heating, photo-thermal, temperature, Raman, phonons, heat conduction, phase transition, finite element modeling

1. Introduction

Nanostructures with thermal conductivities k two or three order of magnitude lower than that of their bulk counterparts have been recently pointed out as a new thermal insulating nanomaterials with unique thermal, mechanical and electrical properties. Low heat conductive composite semiconducting nanoparticles (NPs) are currently used [1] and envisioned [2] as heat insulators for thermal management, thermoelectric energy conversion and optoelectronic devices where phonon scattering can be tailored by controlling NP sizes, matrix material surrounding the NPs and substrate on which the NPs are deposited.

Colloidal NPs can be uniformly deposited on a flat substrate surface by spin coating, which requires highly concentrated NP solutions with viscous organic matrix [3], electrophoretic deposition techniques with

Preprints (www.preprints.org) | NOT PEER-REVIEWED | Posted: 17 August 2021 doi:10.20944/preprints202108.0362.v1

required electrically conductive surface [4], and centrifugation [5]. Drop casting, on the other hand, is a viable alternative bottom-up technique for simple and inexpensive fabrication of thin nanogranular solid films with limited controllability, which has the potential to become a large-scale coating method. This technique is widely used to fabricate thermoelectrics [6] and hybrid polymer insulating films [7].

Photothermal (PT) phenomena are related to heating effects induced by absorbed photons in bulk, thin film and nanostructured materials. The corresponding non-destructive PT methods are employed to heat a sample and the resulting spatial temperature distribution can be used for assessment of thermal conductivity and other thermal properties of the sample material. When it comes to probe thermal transport properties of NP-based films, it is sufficient to use mild laser powers in contrast to the case of bulk materials which would require much higher laser power inputs. To study heat propagation properties in nanostructured materials large variety of PT techniques, such as Raman spectroscopy [8], thermoreflectance [9], spectral radiometry [10] and others have been employed.

In addition to assessment of thermal properties, the PT effects are also utilized in variety of critical applications ranging from thermal imaging [11], PT therapy [12] to hyperthermia for cancer therapy and theranostics [13]. In particular, porous Si (Por-Si) and Si NPs are also attractive for PT therapeutic applications due to their biocompatibility, biodegradability, high surface area and controllable pore diameter [14].

Micro-Raman spectroscopy is known to be a non-destructive and highly sensitive PT technique widely used to study various kinds of non-metallic materials including NPs via probing their phonon vibrational properties and local photo-induced temperature. In this technique, the laser light is used simultaneously for sample heating and for recording of temperature dependent Raman spectra [15]. Heat transport properties of bulk single crystalline Si at high temperatures, Si nanofilm on substrate [16] and thick porous Si layers [17] were studied by means of this technique. Spectral shift of a Raman peak ensured by the laser-induced temperature rise can be used to extract thermal conductivity of heated materials. In particular, thermally anisotropic 2D materials such as Si membranes have been extensively studied where the in-plane heat conduction is much stronger than the cross-plane one [18]. 1D heat conductive structures, such as single Si nanowires with diameters ≤ their phonon mean free paths (l_{MFP}) exhibit suppressed heat conductivities due to phonon boundary scattering [19].

Low power CW laser-induced heating of Si NPs causes softening of the first-order Raman Si-Si transverse optical phonon mode accompanied by a decrease in the corresponding phonon lifetimes [20], while the same Raman shift was observed for bulk crystalline Si heated at substantially higher incident laser powers [21] because bulk Si is much more heat conductive compared to Si NPs. Strong thermal stress causes a singlet-doublet splitting of the Raman peaks into LO and TO phonons, which leads to the phase transition provoking asymmetric broadening and spectral downshift of the Raman peak [22]. Heating of the NPs can actually be quite significant even at mild laser irradiating powers leading to large phonon softening and spectral broadening accompanied by the decay of optical phonon lifetime and pronounced interatomic potential's anharmonicity in the form of 3 and 4-phonon processes [23].

To the best of our knowledge, the thermal transport in drop-casted substrate-supported randomly packed Si nanogranular films with defined NP sizes and spherical shapes, have never been studied before compared to other various types of *nanostructurally voided* Si films ranging from low porosity pressure sintered nanostructured bulk Si (sint-Si) [24-28], crystalline porous Si (c-por-Si) [29-48], amorphous porous Si (a-por-Si) [49-52], crystalline porous Si nanowire (c-por-Si NW) films [53-56] to c-por-Si membranes [57,58]. As opposed to mainly top-down fabrication methods [29-48], the bottom-up approach, such as drop-casting, used

 doi:10.20944/preprints202108.0362.v1

in the present work, has shown to be scalable, simple and cost-effective way to produce nanogranular medium, i.e. new type of nanostructurely voided Si films.

In this paper, we report PT effects observed by means of the micro-Raman spectroscopy in Si nanogranular films with different thicknesses formed by NPs with average size of (100±50) nm deposited on a silica-based glass substrate. The films are inherently voided due to the presence of air inclusions between the stacked NPs. The photo-induced temperature growth estimated by the micro - Raman measurements was correlated with finite difference time domain (FDTD) simulation of the absorbed laser light and steady-state heat transport finite element modeling (FEM) results. Such correlation procedure allowed estimation of thermal conductivities of our drop-casted Si nanogranular thin films having various thicknesses. Measured heat conductivities are compared with those obtained on other *nanostructurely voided* Si-based materials and discussed from the point of view of their potential heat insulating and thermoelectric applications.

2. Materials and Methods

2.1. Sample preparation

The initial pure, highly crystalline Si NP powders with diameters of 100±50 nm (SkySpring Nanomaterials) were prepared by chemical vapor deposition (CVD). Then, the powders were dispersed in distilled water to obtain colloids with different concentrations (3 – 30 mg/mL) and sonicated for 60 minutes at 50 W of sonication power at a rate of 40 kHz to avoid large particle conglomerations. In our bottom-up approach, the colloidal NPs were drop-casted on a glass substrate and dried to obtain films with various thicknesses (2 – 50 μm) at room temperature.

Preprints (www.preprints.org) | NOT PEER-REVIEWED | Posted: 17 August 2021 doi:10.20944/preprints202108.0362.v1

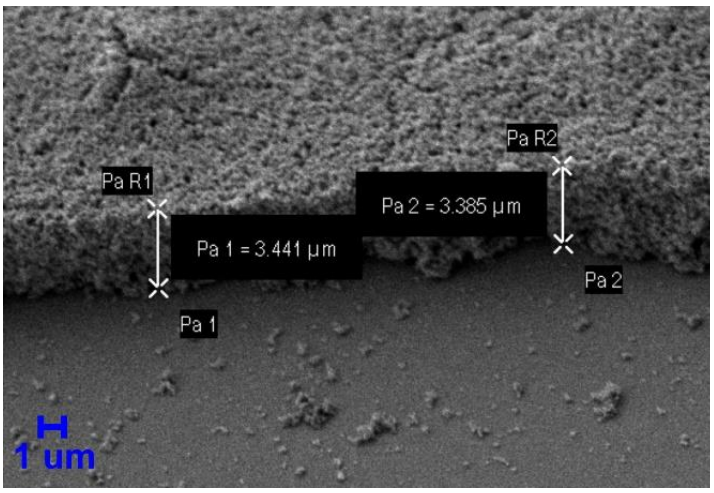

(a)

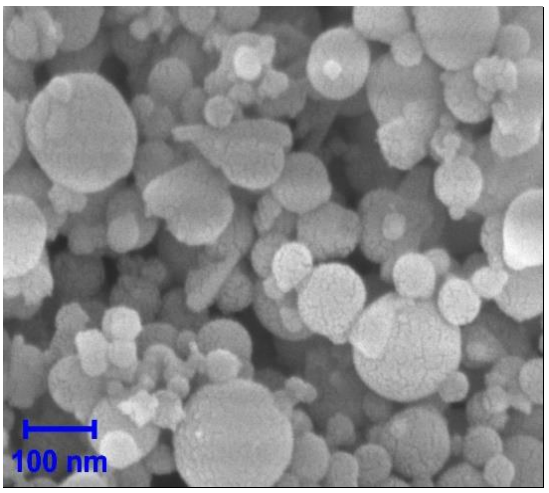

(b)

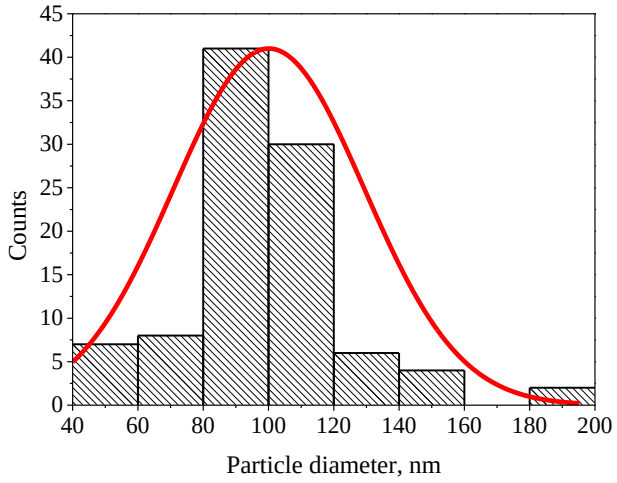

(c)

Figure 1. SEM images of (a) Si nanogranular film and closer view of (b) Si NPs within a film with a typical NP size of 100 ± 50 nm (c).

Figure 1a presents a tilted to 45 degree cross-section image of a typical NP film obtained by scanning electron microscopy (SEM) at relatively low magnification. Figure 1b shows SEM image of a closer look on a typical part of the dried colloidal Si NPs within the formed film sample with NP sizes ranging from 50 to 150 nm. As shown in Figure 1c, the NP size distribution histogram obtained after ImageJ processing of the SEM images among counted 100 NPs.

2.2. Micro-Raman spectroscopy.

Laser-induced heating was implemented by CW *Laser Quantum Torus* diode-pumped solid-state 532 nm single longitudinal mode laser beam focused on Si NP film samples down to a spot of 2 μm diameter by

Preprints (www.preprints.org) | NOT PEER-REVIEWED | Posted: 17 August 2021 doi:10.20944/preprints202108.0362.v1

OptoSigma 20x numerical aperture (NA = 0.45) lens objective. Simultaneous micro-Raman spectral measurements on the laser heated samples were performed in real time using Sol Instruments Nanofinder 30 confocal Raman microscope (with 35 cm focal length spectrograph) coupled to iCCD camera from Andor iStar (Oxford Instruments) operating in static mode. Diffraction grating having 1800 grooves/mm groove density yielded spectral resolution of 1.4 cm^{-1} . The pixel size on the iCCD camera and entrance slit to the spectrometer were 13 and 150 μm, respectively. All reported intensities, positions and linewidths of measured Raman peaks are the results of the Lorentzian fitting.

2.3. Local temperature measurements.

Local laser-induced temperature T was determined from measured Raman Stokes/anti-Stokes integrated intensity ratio, I_S / I_{AS} [21]:

$$\frac{I_s}{I_{AS}} = \frac{(\alpha_I + \alpha_{AS})}{(\alpha_I + \alpha_S)}\left(\frac{\omega_S}{\omega_{AS}}\right)^3 \frac{S(\omega_I, \omega_S)}{S(\omega_I, \omega_{AS})} e^{\frac{\hbar\omega_0}{k_B T}} \quad (1)$$

where, I_S and I_{AS} refer to the integrated intensities of the Stokes and anti-Stokes bands at the same incident laser power. The ratio is proportional to the Boltzmann factor $e^{\frac{\hbar\omega_0}{k_B T}}$; ω_0 – is the phonon frequency; ω_S, ω_{AS} and ω_I are the Stokes, anti-Stokes and incident light photon frequencies, respectively; α_S, α_{AS} and α_I are the optical absorption constants at corresponded light photon frequencies; $S(\omega_I, \omega_S)$ and $S(\omega_I, \omega_{AS})$ are the Raman cross-sections of inelastically scattered photons for Stokes and anti-Stokes sides, respectively. The scattering intensities of both (Stokes and anti Stokes) spectral peaks depend on the phonon populations of the initial states of the material, which in turn depend on the temperature. At thermodynamic equilibrium, the lower state will be more populated than the upper state. Therefore, the rate of transitions from the more populated lower state to the upper state (Stokes transitions) will be higher than in the opposite direction (anti-Stokes transitions).

2.4. FDTD Electromagnetic and FEM Heat modeling.

To describe and quantitatively estimate light absorption in our films, the FDTD is used to solve Maxwell's equations in the time domain on a discreate spatial and temporal grid cell (Yee cell), where the derivatives in both time and space are handled with finite differences and are second order accurate when the grid is uniform [59]:

$$\frac{d}{dt}\vec{E}^n = \frac{\vec{E}^{n+\frac{1}{2}} - \vec{E}^{n-\frac{1}{2}}}{\Delta t} + 0\,(\Delta t^2) \quad (2)$$

$$\frac{d}{dx}\vec{E}_i = \frac{\vec{E}_{i+\frac{1}{2}} - \vec{E}_{i-\frac{1}{2}}}{\Delta x} + 0\,(\Delta x^2) \quad (3)$$

where $\vec{E}_i$ is the electric field vector in one dimensional derivative. The second and third dimensional derivatives: $\vec{E}_j$, $\vec{E}_k$ as well as three dimension time and space derivatives for magnetic field $\vec{H}$ are solved in the same way. Calculations are interleaved in both space and time, but E and H are not calculated at the same point in time, as they must be offset by one half time step as schematically indicated below:

$$\vec{H}^0 \rightarrow \vec{E}^{\frac{1}{2}} \rightarrow \vec{H}^1 \rightarrow \vec{E}^{\frac{3}{2}} \rightarrow \vec{H}^2 \rightarrow \vec{E}^{\frac{5}{2}} \rightarrow \vec{H}^3 \ldots \quad (4)$$

Preprints (www.preprints.org) | NOT PEER-REVIEWED | Posted: 17 August 2021 doi:10.20944/preprints202108.0362.v1

The fundamental simulation quantities were calculated at each cubic mesh point, which was chosen to be 7 nm. Size distribution of NPs shown in Figure 1c were taken into account in our simulation. A random localization of the NPs forming the nanogranular thin film was considered. Physical properties of Si and SiO_2 were taken from Lumerical software material libraries (ANSYS, Inc.) for Si NPs and glass substrate, respectively.

As Heat Transfer solver uses FEM, main simulation quantities are calculated at each mesh vertex. Tetrahedral mesh size used for the 3D heat transport simulation was chosen to be in 0.1 – 2μm range for the corresponding film thickness range of 2 – 50 μm. Since CW laser beam was used for sample heating, the steady state Fourier heat conduction equation was solved [60]:

$$-[\frac{d}{dx}(k\frac{dT}{dx})+\frac{d}{dy}(k\frac{dT}{dy})+\frac{d}{dz}(k\frac{dT}{dz})] = Q \quad (5)$$

where k is the thermal conductivity, T is the local temperature and Q is the applied heat energy density transfer rate [W/m^3] defined by the incident laser radiation heating source.

3.Results and discussion

3.1. FDTD modeling of light penetration

When nanogranular films are illuminated some of incident photons are scattered by Si NPs while others are absorbed and the both processes contribute to the extinction coefficient [61]. In our work the laser light penetration through the Si NP films was simulated using a 3D Maxwell's Solver module of Lumerical FDTD software (ANSYS, Inc.). The simulated 4 μm thick Si NP film with 1 μm × 1 μm lateral surface area on a 4 μm thick silica glass substrate is shown in Figure 2a. Size distribution of Si NPs forming the voided film and corresponding to the data shown in Figure 1 was taken into account. The morphological structure of simulated Si nanogranular film was based on the SEM image processing performed by the ImageJ software with estimated porosity of 0.7 (SEM images before and after ImageJ processing are shown in Figure S1 in Supplementary Materials). The Si NP film/silica substrate is considered to be illuminated by an electromagnetic plane wave with 532 nm wavelength polarized in the direction ($\vec{P}$) parallel to the Si NP film/silica interface. The plane wave with the square of 1.6μm×1.6μm propagates in the direction of wavevector $\vec{k}$ perpendicular to the Si NP film/silica interface.

Preprints (www.preprints.org) | NOT PEER-REVIEWED | Posted: 17 August 2021 doi:10.20944/preprints202108.0362.v1

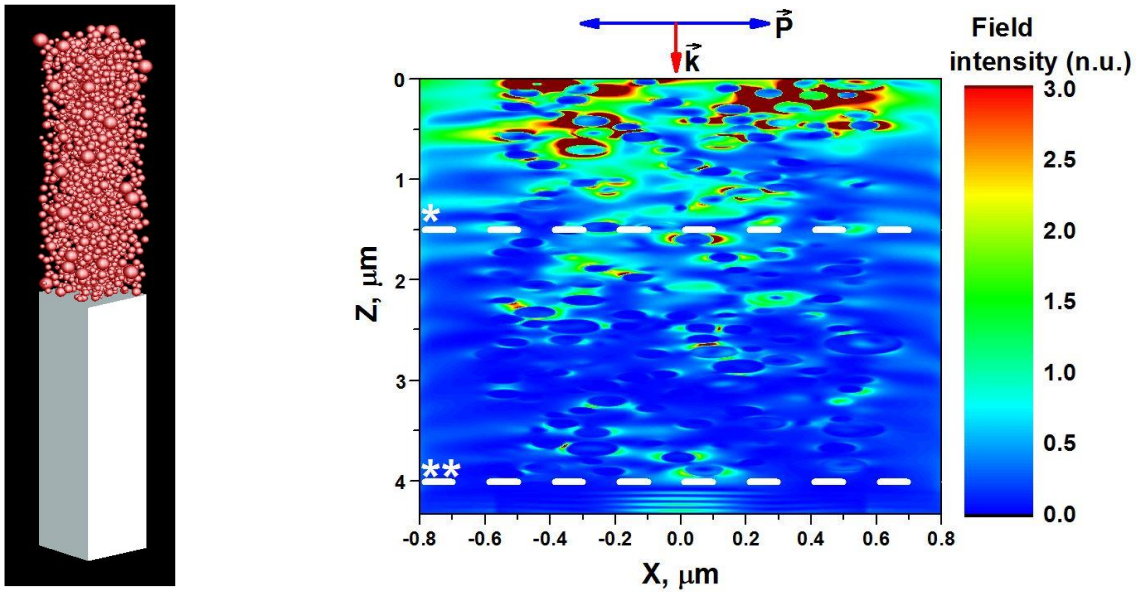

(a) **(b)**

Figure 2. FDTD simulated (a) –nanogranular porous Si NP film on a continuum SiO_2 glass substrate and (b) in-depth distribution of in-coming light (532 nm wavelength) field intensity in the nanogranular porous Si NP film (70% porosity, 4 μm depth (along z-direction) and 1.6 μm x 1.6 μm lateral area within xy-plane with the laser beam diameter (2 μm) fitting into this lateral area). The incident laser beam is shown with wave-vector $\vec{k}$ and polarization $\vec{P}$.* - absorption depth of the incoming light (532 nm), ** - porous Si NP film / silica glass substrate interface.

Figure 2b shows an example of the spatial distribution of the normilized incoming light intensity (E^2/E_0^2), where E is the magnitude of local transmitted electric field and E_0 is the magnitude of the incoming electric field along the depth of the Si NP film. Due to light absorption by Si NPs, the incoming light field intensity decays exponentially along the z-axis. The absorption depth (indicated by *-level in Figure 2b) at which the incident light intensity was reduced by factor of e, was estimated to be about 1.5 μm. This estimation is confirmed by in-depth distribution of the absorbed power density (see Figure S2 in Supplementary Information part), which is mainly concentrated in the near surface region. The light field intensity is much higher inside air voids (scattered light) than within the NPs.

3.2.Laser-induced phase transition in Si nanogranular films

Laser induced heating has a significant effect on phase transformation in Si nanostructures [22, 62]. At room temperature, the cubic phase (c-Si) exhibits diamond-like cubic structure where each Si atom is distant from its four nearest neighbors at 2.73 Å.

Preprints (www.preprints.org) | NOT PEER-REVIEWED | Posted: 17 August 2021 doi:10.20944/preprints202108.0362.v1

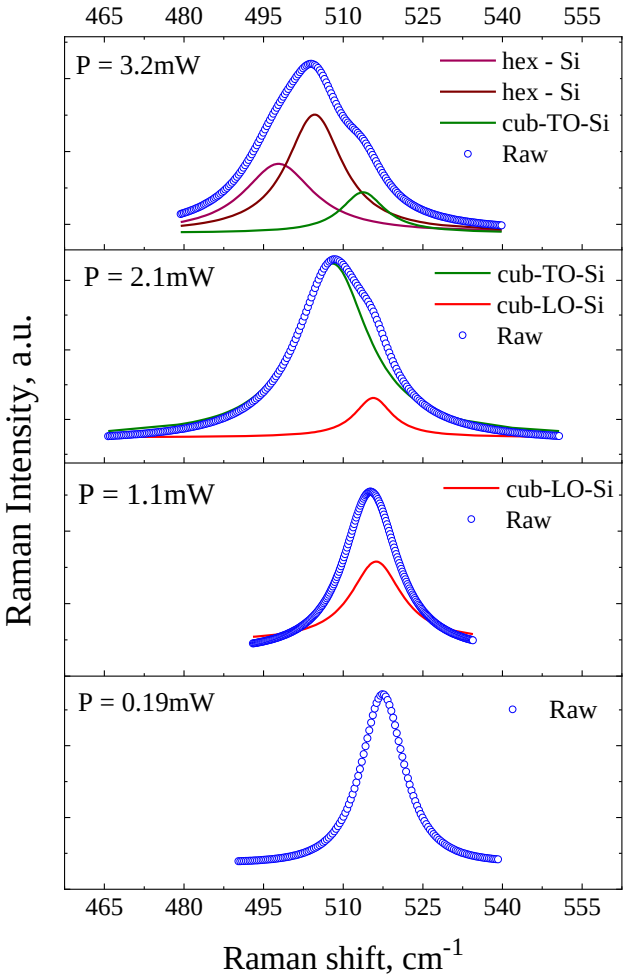

Figure 3. Deconvoluted Raman spectra of the films formed by Si NPs with average size of 100 nm demonstrating a photo-induced phase transition from the cubic to hexagonal one.

At a threshold laser power, resulting in a maximal thermally induced stress, a photo-induced structural relaxation in the overheated part of Si nanostructures leads to formation of the new hexagonal (hex-Si) phase characterized by Raman bands centered near 504 and 497 cm^{-1} and differing from the well-known cubic lattice with the Raman peak at 520 cm^{-1} at room temperature. This phase transition is supposed to be not purely thermally induced but also photo-induced. Formation of the hex-Si phase is accompanied by absorption of electromagnetic radiation and a reduction of the overall mechanical stresses and, consequently, by partial quenching of the splitting between LO and TO phonon modes[22].

Figure 3 illustrates Lorentzian fitted Raman spectra of our Si NP films. The Raman bands obtained at laser power of 2.1 mW and centered near 515 and 507 cm^{-1} correspond, respectively, to the LO and TO phonon modes of cubic c-Si under photo-thermal and mechanical stresses caused by a temperature gradient through Si NP films. At the threshold laser power of 3.2 mW, the photo-induced structural relaxation in the overheated part of Si NPs leads to formation of the hexagonal (hex-Si) phase characterized by Raman bands centered at 504 and 497 cm^{-1}.

Preprints (www.preprints.org) | NOT PEER-REVIEWED | Posted: 17 August 2021 doi:10.20944/preprints202108.0362.v1

3.3.Laser induced heating and thermal conductivity of Si nanogranular films.

As seen from Figure 4a, the main Raman peak of the heated Si nanogranular films attributable to the cubic Si LO phonon mode at ~ 519 cm^{-1} shifts towards lower phonon frequencies when the laser power increases. The frequency shifts of the Stokes and anti-Stokes peaks are symmetric with respect to the Rayleigh line because they correspond to the energy difference between the same upper and lower resonant states [63]. A laser heating-induced red-shift of the Raman peak as high as 20 cm^{-1} over 0.07-3.2 mW range of the incident laser powers is also accompanied by a characteristic increased spectral line broadening.

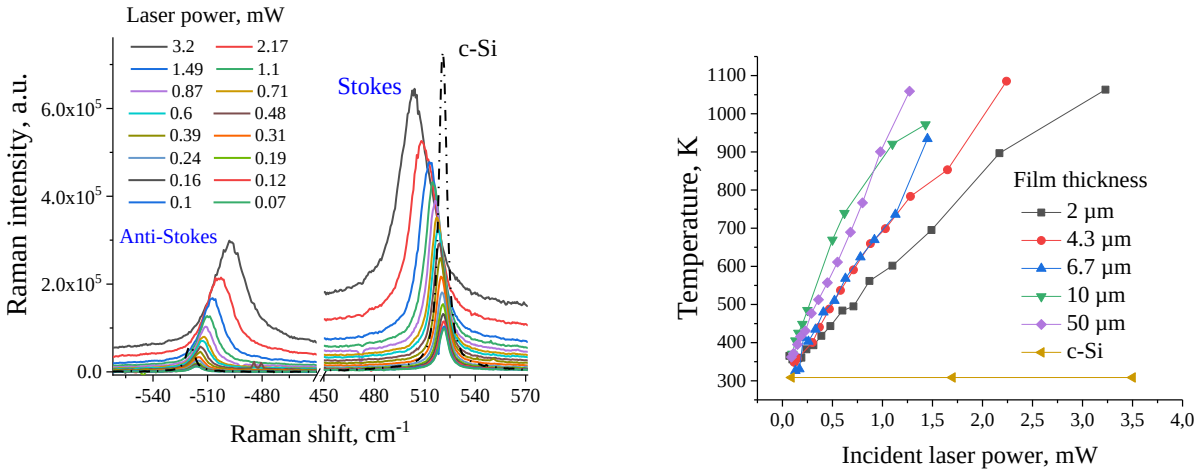

(a) **(b)**

Figure 4. (a) Measured Stokes and ant-Stokes Raman speca at various laser powers and (b) corresponding laser induced temperature rises of the Si NP films with various thicknesses and a bulk crystalline silicon substrate (c-Si).

Figure 4b illustrates laser-induced temperature evolution for the films of different thicknesses. The thinner films are less heated than the thicker ones due to more efficient heat sinking toward the silica glass substrates on which the films are deposited. The similar effect was also earlier observed for polycrystalline silicon discs on fused silica and sapphire substrates [64]. Thus, an appreciable amount of laser-induced heat will easily "sink" from the thinnest 2 μm-thick film toward the bulk glass substrate. At film thicknesses > 2 μm, the effect of the heat-sinking to the substrate becomes weaker and leads to the higher temperature excursions within the films. We observed the expected temperature increase with the rise of incident laser power for all film thickness. The laser-induced local heating has also resulted in the enhancement of thermal radiation background as evidenced from the more significant rise of the baseline on the Stokes side compared to the anti-Stokes side of the recorded Raman spectra as shown in Figure 4a.

Preprints (www.preprints.org) | NOT PEER-REVIEWED | Posted: 17 August 2021 doi:10.20944/preprints202108.0362.v1

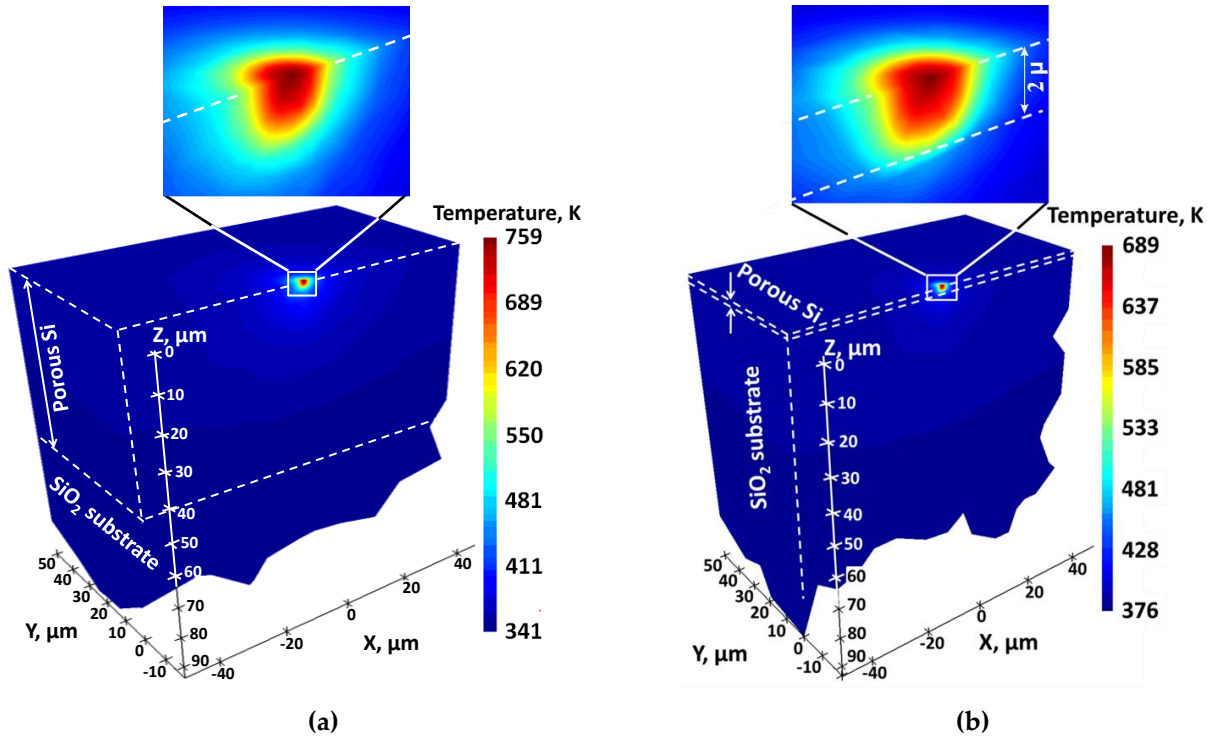

Figure 5. In-depth temperature distribution for porous Si NP films deposited on 1 mm thick SiO_2 glass substrate with the film thickness of (a) 50 µm and (b) 2 µm. Film heating is induced by a 532 nm wavelength laser beam of 2 µm diameter focused on the film surface.

The temperature-induced effect on vibrational states in bulk c-Si and Si NP films can be estimated from the Raman peak's position and linewidth. Indeed, a higher anharmonicity in the vibrational potential energy for the Si NP films can be noticed in comparison with bulk c-Si irradiated at the same laser powers. Because of anharmonicity of the lattice forces, the incident photons can interchange energy with the phonon lattice modes and therefore maintain thermal equilibrium. Besides, an increase of the interatomic lattice parameter leads to interatomic bonds weakening. The spectral linewidth scales reciprocally with the lifetime of the optical phonon mode decay processes. The thermal interaction increases with the temperature rise, causing the suppression of mean phonon free path (l_{MFP}) with a corresponding decay in phonon lifetime [21, 65].

The heat conduction through a Si NP film deposited on 1 mm-thick silica substrate with surface area of 100 µm × 100 µm was numerically described by means of a 3D Heat Transport FEM Solver module of Lumerical software (ANSYS, Inc.). The local temperatures estimated from micro-Raman spectroscopy and achieved inside a near-surface cylindrical region of the laser spot with 2 µm diameter and 1.5 µm optical penetration depth in Si NP films of various film thicknesses (2 – 50 µm) were fitted by the FEM. Heat flows across the films is deduced from the Raman measurements in Figure 4b to remain constant at low temperatures (T<700K). The dependence of the heat flux on T is expected to be nonlinear at higher (T>700K) temperatures due to: (i) possible temperature dependent structural variations of the films as well as (ii) temperature dependent thermal conductivities of the Si NPs. Thus, the FEM modeling of the laser-induced heat conduction is performed for the low temperature region to avoid any non-linear behavior of the relation between incident powers and resulting temperatures.

 doi:10.20944/preprints202108.0362.v1

The maximum temperatures measured by the Raman technique and determined along the optical penetration depth of 1.5 μm for 532 nm laser beam were fitted for 50 and 2 μm-thick Si nanogranular films, as shown in Figure 5a and 5b, respectively. The single fitting parameter allowing a precise correlation between the experimentally measured and theoretically calculated temperatures was thermal conductivity of the films. The resulted 3D-temperature distributions are also numerically predicted for each case. For the *thermally thick* substrate shown in Figure 5a, the film thickness (50 μm) being much larger than the laser beam diameter (2 μm) results in the almost perfect semispherical temperature isotherms implying that the laser beam focused at the sample surface mimics a point heating source. The temperature gradient is mainly localized within the subsurface depth of 5 μm. In opposite, as shown in Figure 5b, for the *thermally thin* Si nanogranular films with thickness of 2 μm, the temperature profiles strongly impacted by the close proximity of the Si nanogranular film/silica interface have an irregular shape with clearly expressed flat heat front parallel to the interface.

Taking into account geometry of the Si NP film/silica structure and of the laser-induced hot spot at the film surface as well as absorbed laser power value, one can fit the temperatures reached in the heated spots by thermal conductivity values of the Si NP films. The thermal conductivities determined by this approach for our Si nanogranular films as a function of different film thicknesses are given in Figure 6 and are compared with those reported earlier for other types of *nanostructurely voided* Si films. In our films, the thermal conductivities decrease with the rising film thickness, except for 50 μm thick film, where Si NPs are assumed to be more tightly packed resulting in an increase of the neck areas between interconnected Si NPs and in a global reduction of the effective film porosity. The thin layers are more thermally conductive than the thick ones, because the former are more affected by the heat-sinking glass substrate. Besides, with the reduction of the film thickness, the in-plane heat conduction distribution becomes substantial compared to the cross-plane thermal conductivity. Therefore, it is essential to compare heat conduction in various nanostructurely voided Si materials as function of their thicknesses. Moreover, as can be seen from Figure 6 and Supplementary Table S1, the thermal conductivity can be controlled by means of different etching techniques leading to formation of various porous morphologies. For example, n-type thick porous Si samples have multi-porous (nano, meso, micro) and p+, p-type samples have single porous morphologies [30]. In general, measured thermal conductivities (0.53 - 0.19 W/mK) of our Si nanogranular films are in the range of the *lowest* thermal conductivity values of *nanostructurely voided* Si films [29-48], Si nanowire films [53-56], amorphous porous Si films [49-52], crystalline porous Si membranes [57,58] and sin-Si NP tablets [24-28].

Preprints (www.preprints.org) | NOT PEER-REVIEWED | Posted: 17 August 2021 doi:10.20944/preprints202108.0362.v1

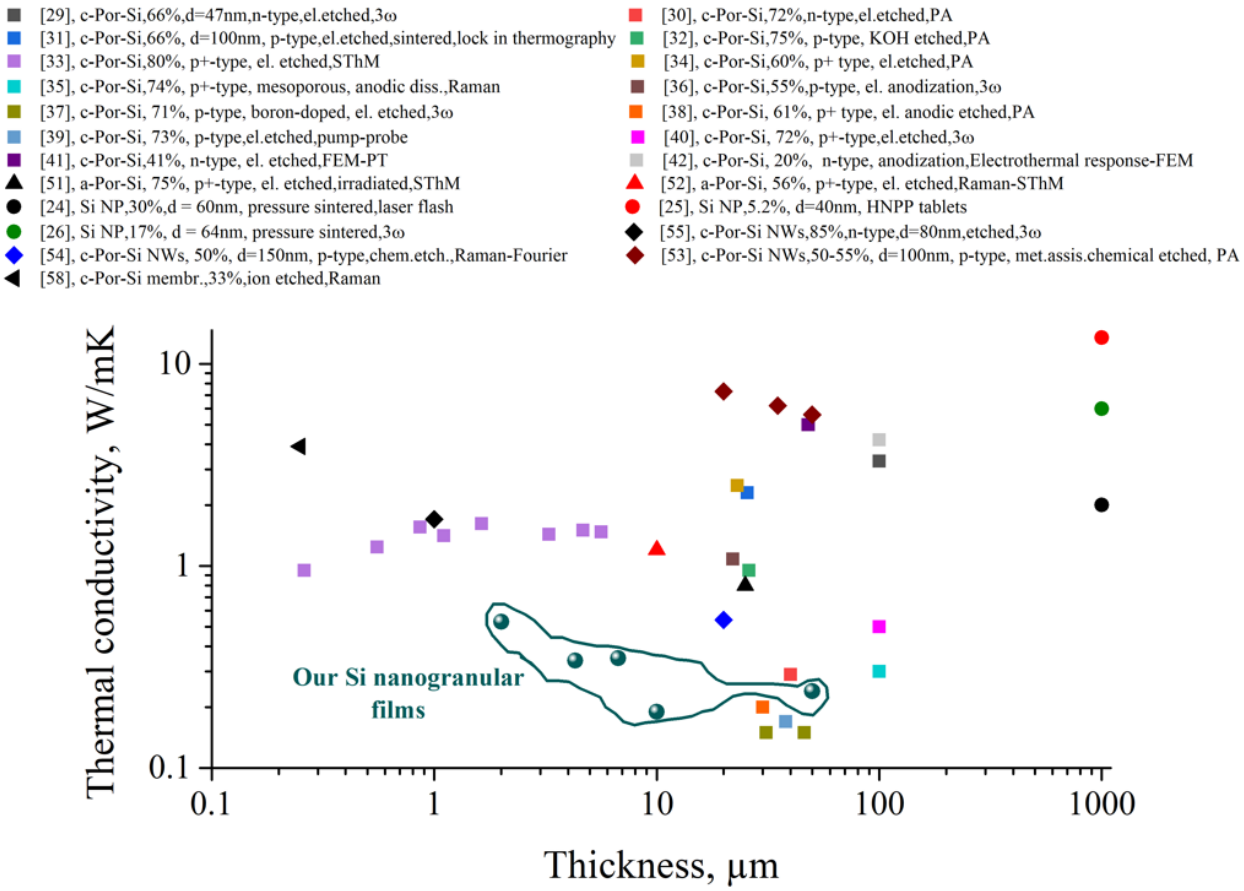

Figure 6. Measured thermal conductivity values of our Si *nanogranular* films with 70 % porosity in comparison with other types of *nanostructurally voided* Si films (taken from literature) versus different film thicknesses.

Additionally, when the size of a nanostructure becomes comparable or smaller than l_{MFP}, phonons collide with intergranular boundaries much more often than in single crystalline bulk materials. This additional collision mechanism increases the resistance to heat flow between NPs and thus reduces the effective thermal conductivity of Si NP films compared to bulk c-por-Si [66,67]. l_{MFP} decreasing with the particle size, leads to the reduction of the effective thermal conductivity [68]. Finally, a long exposure of Si NPs in an open-air environment can result in their increased surface oxidation causing formation of SiO_2 shells and leading to an additional decrease of their thermal conductivities [69].

4.Conclusions

We have investigated the PT effect and heat conductive properties of drop-casted Si nanogranular films by means of the micro-Raman spectroscopy correlated with FDTD optical and FEM heat conduction simulations. The observed photo-induced Raman spectral variations were attributed to the cubic-to-hexagonal structural phase transition. The heat conductivity in the prepared nanogranular Si films was found to be in the range of the lowest thermal conductivities of *nanostructurely voided Si films* including bulk and thin film crystalline and amorphous porous Si structures of various porosity. It was established that: (i) presence of air voids, (ii) additional interface thermal resistance across NP-NP boundaries in our nanogranular Si films, as well as (iii)

NP sizes smaller than mean phonon free path (l_{MFP}) ensure thermal conductivity values of the films which are much lower than that of crystalline bulk Si.

Heating of Si nanogranular films are also heavily influenced by their thicknesses and thermal conductive properties of heat-sinking glass substrate on which the films were deposited, suggesting a major role played by the NP-substrate binding. Besides, glass substrate leads to the increase of thinner films' thermal conductivity, which decreases with the rising of thickness until the negligibility of the substrate effect, which is similar to the case of porous Si films taking into account interface thermal resistance. Tailoring the film thickness, NP size and film porosity within surrounding air matrix by bottom-up drop-casting approach opens avenue for effective control of heat insulating and thermoelectric performance across variety of energy conversion applications of semiconductor NPs.

Supplementary materials: The following available online at **link.** Figure S1: SEM images before and after ImageJ processing for porosity estimation. Figure S2: Absorbed power density (in W/m^3, $\times 10^{15}$) at different depths (z) of 4 μm thick porous Si NPs film on 4 μm thick glass substrate: (a) z = 0.1 μm, (b) z = 1 μm, (c) z = 2 μm, (d) z = 3 μm. Table S1: Room temperature thermal conductivity values of nanostructured porous Si.

Author contributions: Experiment, B.A.K.; simulations, V.L.; writing-original draft preparation, B.A.K, Z.N.U.; writing-review and editing, all authors; funding acquisition, Z.N.U.; All authors have read and agreed to the published version of the manuscript.

Funding: B.A.K and Z.N.U. acknowledge grant funding from Nazarbayev University FDCR grant 110119FD4501, Kazakhstan Ministry of Education & Science grant AP05130446 and state-targeted program BR05236454. G.M. is grateful to Al-Farabi Kazakh National University for a Scholarship in the Postdoctoral Fellowship program.

Acknowledgments: I.V. Lysenko from the Physics Faculty of Kyiv National T. Shevchenko University is acknowledged for his participation in simulation of optical and thermal properties of porous Si films as well as for fruitful discussions.

Conflicts of Interest: The authors declare no conflict of interest.

References:

1. Schierning, G. Silicon nanostructures for thermoelectric devices: A review of the current state of the art. *Phys. Status Solidi A* **2014**, *211*, 1235 - 1249.
2. Elsahati, M.; Clarke, K.; Richards, R. Thermal conductivity of copper and silica nanoparticle packed beds. *International Communications in Heat and Mass Transfer* **2016**, *71*, 96–100.
3. Hong, Y.; Kim, H.; Lee, G.; Kim, W.; Park, J.; Cheon, J.; Koo, J. Controlled two-dimensional distribution of nanoparticles by spin-coating method. *Appl. Phys. Lett.* **2002**, *80*, 844-846.
4. Fernández-Arias, M.; Zimbone, M.; Boutinguiza, M.; Val, J.D.; Riveiro, A.; Privitera, V.; Grimaldi, M.G.; Pou, J. Synthesis and Deposition of Ag Nanoparticles by Combining Laser Ablation and Electrophoretic Deposition Techniques. *Coatings* **2019**, *9*, 571.
5. Markelonis, A.R.; Wang, J.S.; Ullrich, B.; Wai, Ch.M.; Brown, G.J. Nanoparticle film deposition using a simple and fast centrifuge sedimentation method. *Appl Nanosci*. **2015**, *5*, 457–468.
6. Yabuki, H.; Yonezawa, S.; Eguchi, R.; Takashir, M. Flexible thermoelectric flms formed using integrated nanocomposites with single-wall carbon nanotubes and Bi_2Te_3 nanoplates via solvothermal synthesis. *Scientific Reports* **2020**, *10*, 1 - 11.

7. Toshima, N.; Oshima, K.; Anno, H.; Nishinaka, T.; Ichikawa, S.; Iwata, A.; Shiraishi, Y. Novel Hybrid Organic Thermoelectric Materials: Three-Component Hybrid Films Consisting of a Nanoparticle Polymer Complex, Carbon Nanotubes, and Vinyl Polymer. *Adv. Mater*. **2015,** *27*, 2246 - 2251.
8. Ishii, S.; Higashino, M.; Goya, S.; Shkondin, E.; Tanaka, K.; Nagao, T.; Takayama, O.; Murai, S. Extreme thermal anisotropy in high-aspect-ratio titanium nitride nanostructures for efficient photothermal heating. *Nanophotonics* **2021**, *10*, 1487–1494.
9. Abdullaev, A.; Chauhan, V.S.; Muminov, B.; O'Connell, J.; V. Skuratov, V.A.; Khafizov, M.; Utegulov, Z.N. Thermal transport across nanoscale damage profile in sapphire irradiated by swift heavy ions, *Journal of Applied Physics* **2020**, *127*, 035108.
10. Salazar, A.; Fuente, R.; Apinaniz, E.; Mendioroz, A.; Celorrio, R. Simultaneous measurement of thermal diffusivity and optical absorption coefficient using photothermal radiometry. II Multilayered solids. *Journal of Applied Physics* **2011**, *110*, 033516.
11. Murphy, J.C.; Aamodt, L.C. Optically detected photothermal imaging. *Appl. Phys. Lett.* **1981**,*38*, 196 - 198.
12. Zhi, D.; Yanga, T.; O'Haganb, J.; Zhanga, Sh.; Donnelly, R.F. Photothermal therapy. *J. of Controlled Release* **2020**, *325*, 52 – 71.
13. Kaur, P.; Aliru, M.L.; Chadha, A.S.; Asea, A.; Krishnan, S. Hyperthermia using nanoparticles – Promises and pitfalls. *Int J Hyperthermia* **2016**, *32*, 76–88.
14. Xu, W.; Tamarov, K., Fan, L.; Granroth, S.; Rantanen, J.; Nissinen, T.; Peräniemi, S.; Uski, O.; Hirvonen, M.; Lehto, V. Scalable Synthesis of Biodegradable Black Mesoporous Silicon Nanoparticles for Highly Efficient Photothermal Therapy. *ACS Appl. Mater. Interfaces* **2018**, *10*, 23529−23538.
15. Li, Q.; Xia, K.; Zhang, J.; Zhang, Y.; Li, Q.; Takahashi, K.; Zhang, X. Measurement of specific heat and thermal conductivity of supported and suspended graphene by a comprehensive Raman optothermal method. *Nanoscale* **2017**, *9*, 10784 – 10793.
16. Poborchii, V.; Uchida, N.; Miyazaki, Y.; Tada, T.; Geshev, P.I.; Utegulov, Zh.N.; Volkov, A. A simple efficient method of nanofilm-on-bulk-substrate thermal conductivity measurement using Raman thermometry. *International Journal of Heat and Mass Transfer* **2018**, *123*,137–142.
17. Périchon, S.; Lysenko, V.; Remaki, B.; Barbier, D.; Champagnon, B. Measurement of porous silicon thermal conductivity by micro-Raman scattering. *J. of Appl. Phys.* **1999**, *86*, 4700 - 4702.
18. Chavez-Angel, E.; Reparaz, J.S.; Gomis-Bresco, J.; Wagner, M.R.; Cuffe, J.; Graczykowski, B.; Shchepetov, A.; Jiang, H.; Prunnila, M.; Ahopelto, J.; Alzina, F.; Sotomayor Torres, C.M. Reduction on the thermal conductivity in free-standing silicon nano-membranes investigated by non-invasive Raman thermometry. *Apl.Materials* **2014**, *2*, 012113.
19. Doerk, G.S.; Carraro, C.; Maboudian, R. Single Nanowire Thermal Conductivity Measurements by Raman Thermography. *ACS Nano* **2010**, *4*, 4908–4914.
20. Mishra, P.; Jain, K.P. Temperature-dependent Raman scattering studies in nanocrystalline silicon and finite-size effects. *Phys. Rev. B – Condensed Matter and Materials Physics* **2000**, *62* , 14790- 14795.
21. Balkanski, M.; Wallis, R.F.; Haro, E. Anharmonic effects in light scattering due to optical phonons in silicon. *Phys. Rev. B* **1983**, *28*, 1928-1934.
22. Rodichkina S.; Lysenko V.; Belarouci A.; Bezverkhyy I.; Chassagnon R.; Isaiev M.; Nychyporuk T.; Timoshenko V. Y. Photo-Induced Cubic-To-Hexagonal Polytype Transition in Silicon Nanowires. *Cryst. Eng. Comm.* **2019**, *21*, 4747–4752.
23. Popovic, Z.V.; Dohcevic-Mitrovic, Z.; Konstantinovic, M.J.; Scepanovic, M. Raman scattering characterization of nanopowders and nanowires (rods). *J. Raman Spectrosc*. **2007**, *38*, 1538–1553.

24. Ashby, Sh.P.; Bian, T.; Ning, H.; Reece, M.J.; Chao, Y. Thermal Diffusivity of SPS Pressed Silicon Powders and the Potential for Using Bottom–Up Silicon Quantum Dots as a Starting Material. *J. Electr.Mat.* **2015,** 44, 1931 – 1935.
25. Suzuki, T.; Ohishi, Y.; Kurosaki, K.; Muta, H.; Yamanaka, S. Thermal Conductivity of Size-Controlled Bulk Silicon Nanocrystals Using Self-Limiting Oxidation and HF Etching. *Applied Physics Express* **2012**, *5*, 081302.
26. Wang, Zh.; Alaniz, J.E.; Jang, W.; Garay, J.E.; Dames, Ch. Thermal Conductivity of Nanocrystalline Silicon: Importance of Grain Size and Frequency-Dependent Mean Free Paths. *Nano Lett.* **2011**, *11*, 2206–2213.
27. Zhu, G.H.; Lee, H.; Lan, Y.C.; Wang, X.W.; Joshi, G.; Wang, D.Z.; Yang, J.; Vashaee, D.; Guilbert, H.; Pillitteri, A.; Dresselhaus, M.S.; Chen, G.; Ren, Z.F. Increased Phonon Scattering by Nanograins and Point Defects in Nanostructured Silicon with a Low Concentration of Germanium. *Phys.Rev.Lett*. **2009**, *102*, 2 - 5.
28. Bux, S.K.; Blair, R.G.; Gogna, P.K.; Lee, H.; Chen, G.; Dresselhaus, M.S.; Kaner, R.B.; Fleurial, J. Nanostructured Bulk Silicon as an Effective Thermoelectric Material. *Adv. Funct. Mater*. **2009**, *19*, 2445–2452.
29. Boor, J.D.; Kim, D.S.; Ao, X.; Hagen, D.; Cojocaru, A.; Foll, H.; Schmidt, V. Temperature and structure size dependence of the thermal conductivity of porous silicon. *EPL* **2011**, *96*, 16001.
30. Lettieri, S.; Bernini, U.; Massera, E.; Maddalena, P. Optical investigations on thermal conductivity in n- and p-type porous silicon. *Phys. Stat. Sol. (c) 2*, **2005**, *3418*, 3414–3418.
31. Wolf, A.; Brendel, R. Thermal conductivity of sintered porous silicon films. *Thin Solid Films* **2006**, *513*, 385–390.
32. Amato, G.; Angelucci, R.; Benedetto, G.; Boarino, L.; Dori, L.; Maccagnani, P.; Rossi, A.M.; Spagnolo, R. Thermal Characterisation of Porous Silicon Membranes. *J. Porous Materials* **2000**, *186*, 183–186.
33. Gomes, S.; David, L.; Lysenko, V.; Descamps, A.; Nychyporuk, T.; Raynaud, M. Application of Scanning thermal microscopy for thermal conductivity measurements on meso-porous Si thin films. *J. Phys. D: Appl. Phys.* **2007**, *40*, 6677 – 6683.
34. Benedetto, G.; Boarino, L.; Spagnolo, R. Evaluation of thermal conductivity of porous silicon layers by a photoacoustic method. *Appl. Phys. A* **1997**, *6*, 155 – 159.
35. Lysenko, V.; Perichon, S.; Remaki, B.; Barbier, D.; Champagnon, B. Thermal conductivity of thick meso-porous silicon layers by micro-Raman scattering. *J. Appl. Phys.* **1999**, *86(12)*,6841-5846.
36. Kihara, Y.; Harada, T.; Koshida, N. Precise Thermal Characterization of Confined Nanocrystalline Silicon by a 3w Method. *Jpn. J. Appl. Phys.* **2005**, *44(6A)*, 4084-4087.
37. Gesele, G.; Linsmeier, J.; Drach, V.; Fricke, J.; Arens-Fischer, R. Temperature-dependent thermal conductivity of porous silicon. *J.Phys.D: Appl.Phys.* **1997**, *30*, 2911-2916.
38. Shen, Q.; Toyoda, T. Dependence of thermal conductivity of porous silicon on porosity characterized by photoacoustic technique. *Rev. Sci. Instrum*. **2003**, *74*, 601.
39. Bernini, U.; Lettieri, S.; Maddalena, P.; Vitiello, R.;Francia, G.Di. Evaluation of thermal conductivity of porous silicon layers by an optical pump-probe method. *J.Phys.: Condens.Matter*. **2001**, *13*, 1141-1150.
40. Valalaki, K.; Nassiopoulou, A.G. Improved approach for determining thin layer thermal conductivity using the 3ω method. Application to porous Si thermal conductivity in the temperature range 77–300 K. *J. Phys. D: Appl. Phys*. **2017**, *50*, 195302.
41. Melhem, A.; Meneses, D.D.S.; Andreazza-Vignolles, C.; Defforge, T.; Gautier, G.; Semmar, N. Structural, Optical, and Thermal Analysis of n-Type Mesoporous Silicon Prepared by Electrochemical Etching. *J. Phys. Chem. C* **2015**, *119*, 21443−21451.
42. Siegert, L.; Capelle, M.; Roqueta, F.; Lysenko, V.; Gautier, G. Evaluation of mesoporous silicon thermal conductivity by electrothermal finite element simulation. *Nanoscale Research Letters* **2012**, *7*(427), 1 – 7.

43. Dubyk, K.; Nychyporuk, T.; Lysenko, V.; Termentzidis, K.; Castanet, G.; Lemoine, F.; Lacroix, D.; Isaiev, M. Thermal properties study of silicon nanostructures by photoacoustic technique. *J.Appl.Phys*. **2020**, *127*, 225101.
44. Alvarez, F.X.; Jou, D.; Sellito, A. Pore-size dependence of thermal conductivity of porous silicon: A phonon hydrodynamic approach. *Appl.Phys.Lett.* **2010**, *97*, 033103.
45. Radrianalisoa, J.; Baillis, D. Monte-Carlo simulation of cross-plane thermal conductivity of nanostructured porous silicon films. *J.Appl.Phys*. **2008**, *103*, 053502.
46. Song, D.; Chen, G. Thermal conductivity of periodic microporous silicon films. *Appl. Phys.Lett*. **2004**, *84*, 687.
47. Sellito, A.; Jou, D.; Cimmelli, V.A. A Phenomenological Study of Pore Size Dependent Thermal Conductivity of Porous Silicon. *Acta.Appl.Math*. **2012**, *122*, 435-445.
48. Fang, J.; Pilon, L. Tuning thermal conductivity of nanoporous crystalline silicon by surface passivation. *Appl.Phys.Lett*. **2012**, *101*, 011909.
49. Newby, P.J.; Canut, B.; Bluet, J.; Gomes, S.; Isaiev, M.; Burbelo, R.; Termentzidis, K.; Chantrenne, P.; Frechette, L.G.; Lysenko, V. Amorphization and reduction of thermal conductivity in porous silicon by irradiation with swift heavy ions. *J. Appl. Phys*. **2013**, *114*, 014903.
50. Isaiev, M.; Newby, P.J.; Canut, B.; Tytarenko, A.; Lishchuk, P.; Andrusenko, D.; Gomès, S.; Bluet, J.; Fréchette L.G.; Lysenko, V.; Burbelo, R. Thermal conductivity of partially amorphous porous silicon by photoacoustic technique. *Materials Letters* **2014**, *128*, 71–74.
51. Gomes, S.; Newby, P.; Canut, B.; Termentzidis, K.; Marty, O.; Frechette, L.; Chantrenne, P.; Aimez, V.; Bluet, J.; Lysenko, V. Characterization of the thermal conductivity of insulating thin films by scanning thermal microscopy. *Microelectronics Journal* **2013**, *44*, 1029-1034.
52. Massoud, A.M.; Chapuis, P.O.; Canut, B.; Bluet, J.M. Thermal conductivity of irradiated porous silicon down to the oxide limit investigated by Raman thermometry and scanning thermal microscopy. *J. Appl. Phys*. **2020**, *128*, 175109.
53. Dubyk, K.; Pastushenko, A.; Nychyporuk, T.; Burbeloa, R.; Isaiev, M.; Lysenko, V. Thermal conductivity of silicon nanomaterials measured using the photoacoustic technique in a piezoelectric configuration. *J. Phys. Chem. Solids* **2018**, *126*, 267-273.
54. Isaiev, M.; Didukh, O.; Nychyporuk, T.; Timoshenko, V.; Lysenko, V. Anisotropic heat conduction in silicon nanowire network revealed by Raman scattering. *Appl. Phys. Lett.* **2017**,*110*, 011908.
55. Curtin, B.J.; Fang, W.E.; Bowers, J.E. Highly Ordered Vertical Silicon Nanowire Array Composite Thin Films for Thermoelectric Devices. *Journal of Electronic Materials* **2012**, *41(5),* 887 - 894.
56. Zhao, Y.; Yang, L.; Kong, L.; Nai, M.H.; Liu, D.; Wu, J.; Liu, Y.; Chiam, S.Y.; Chim, W.K.; Lim, C.T.; Li, B.; Thong, J.T.L.; Hippalgaonkar, K. Ultralow Thermal Conductivity of Single-Crystalline Porous Silicon Nanowires. *Adv. Funct. Mater.* **2017**, *27(40)*, 1 – 8.
57. Dettori, R.; Melis, C.; Cartoixa, X.; Rurali, R.; Colombo, L. Model for thermal conductivity in nanoporous silicon from atomistic simulations. *Phys.Rev. B* **2015**, *91*, 054305.
58. Graczykowski, B.; Sachat, A.E.; Reparaz, J.S.; Sledzinska, M.; Wagner, M.R.; Chavez-Angel, E.; Wu, Y.; Volz, S.; Wu, Y.; Alzina, F.; Torres, C.M.S. Thermal conductivity and air-mediated losses in periodic porous silicon membranes at high temperatures. *Nature Communications* **2017**, *8,*415.
59. Lumerical FDTD module.
60. Lumerical Heat module.
61. Jaque, D.; Maestro, M.L.; Rosal, B.D.; Haro-Gonzalez, P.; Benayas, A.; Plaza, J.L.; Rodrıguez, E.M.; Sol´e, J.G. Nanoparticles for photothermal therapies. *Nanoscale* **2014**, *6*, 9494 - 9530.

62. Yukhymchuk, V.O.; Dzhagan, V.M.; Valakh, M.Y.; Klad'ko, V.P.; Gudymenko, O.J.; Yefanov, V.S.; Zahn, D.R.T. In situ photoluminescence/Raman study of reversible photo-induced structural transformation of nc-Si. *Materials Research Express 1* **2014**, *1(4)*, 045905.
63. Iqbal, Z.; Veprek, S. Raman scattering from hydrogenated microcrystalline and amorphous silicon. *J. Phys. C: Solid State Phys.***1982**, *15*, 377-392.
64. Pazionis, G.D.; Tang, H.; Herman, I.P. Raman Microprobe Analysis of Temperature Profiles in CW Laser Heated Silicon Microstructures. *J. of Quantum electronics* **1989**, *25(5)*, 976-988.
65. Han, L.; Zeman, M.; Smets, A.H.M. Raman study of laser-induced heating effects in free-standing silicon nanocrystals. *Nanoscale* **2015**, *7*, 8389-8397.
66. Chen, G. Phonon heat conduction in nanostructures. *Int. J. Therm. Sci.* **2000**, *39*, 471–480.
67. Chantrenne, P.; Lysenko, V. Thermal conductivity of interconnected silicon nanoparticles: Application of Porous silicon nanostructures. *Phys.Rev. B* **2005**, *72*, 035318.
68. Wu, D.; Huanga, C. Thermal conductivity study of SiC nanoparticle beds for thermal insulation applications. *PhysicaE:Low dimensional Systems and Nanostructures* **2020**, *118*, 113970.
69. Poborchii, V.; Tada, T.; Kanayama, T. Giant heating of Si nanoparticles by weak laser light: Optical microspectroscopic study and application to particle modification. *J. Appl. Phys.* **2005**, *97*, 104323.